

Supplementary Information for

Reversing disadvantage to advantage: synthesizing high-quality organometallic halide perovskite nanosheet arrays for humidity sensor

Kuankuan Ren, Le Huang, Shizhong Yue, Shudi Lu, Kong Liu, Muhammad Azam, Zhijie Wang*, Zhongming Wei*, Shengchun Qu*, and Zhanguo Wang

Key Laboratory of Semiconductor Materials Science, Beijing Key Laboratory of Low Dimensional Semiconductor Materials and Devices, State Key Laboratory of Superlattices and Microstructures, Institute of Semiconductors, Chinese Academy of Sciences, Beijing, 100083, China.

Section 1. Additional Experimental Details

Section 2. Additional Figures and Discussions

Section 3. Discussion on the influence of humidity on the sensing performance

Section 4. Discussion on the specificity of the devices

Section 1. Additional Experimental Details

Materials. Lead acetate trihydrate ($\text{PbAc}_2 \cdot 3\text{H}_2\text{O}$, 99%) and Dimethyl Sulfoxide (DMSO) were obtained from Beijing Chemical Reagent Company. Methylammonium iodide ($\text{CH}_3\text{NH}_3\text{I}$, 99.5%), Methylammonium chloride ($\text{CH}_3\text{NH}_3\text{Cl}$, 99.5%), Lead Chloride (PbCl_2 , 99.99%) and Lead Iodide (PbI_2 , 99.99%) were purchased from Xi'an Polymer Light Technology Corp. Ethyleneglycol monomethyl ether ($\text{CH}_3\text{OCH}_2\text{CH}_2\text{OH}$, 98%) was purchased from Xilong Chemical CO.LTD. Isopropanol ($\text{C}_3\text{H}_8\text{O}$, 99.7%) was purchased from Tianjin Fengchuan Chemical Reagent Co. LTD. Poly (3, 4-ethylenedioxythiophene) polystyrene sulfonate (PEDOT: PSS, Clevios PVP. AI 4083) was purchased from Heraeus. Glass substrates were supplied by Zhuhai Kaivo Optoelectronic Tech. Co. LTD, China.

Growth of single crystal halide $\text{CH}_3\text{NH}_3\text{PbI}_{3-x}\text{Cl}_x$ nanosheet arrays. All chemicals were used as received without further purification. The glass substrates were washed with deionized water, acetone, and isopropanol for 30 minutes under ultrasonic environment, respectively. And then the substrates were dried under nitrogen flow and cleaned by ultraviolet ozone for 15 minutes. A buffer layer of high hydrophilous PEDOT: PSS thin film was spin-coated onto the substrate at 3000 rpm for 40 seconds before annealed at 150 °C for 15 minutes, then the temperature was reduced to 65 °C naturally within 15 minutes. Afterwards, the substrate was drop-cast with several tens of microliters of unsaturated ethylene glycol monomethyl ether solution with lead acetate trihydrate, which could spread easily on the PEDOT: PSS layer. The sample was then annealed at 65 °C for 30 minutes in air. After the sample was cooled, it was carefully faced down or faced up in a mixed halide $\text{CH}_3\text{NH}_3\text{I}$ /isopropanol (9 mg/mL) and $\text{CH}_3\text{NH}_3\text{Cl}$ /isopropanol (9 mg/mL) solution (1mL) at room temperature. The reaction was allowed to proceed for 12 to 16 hours to form $\text{CH}_3\text{NH}_3\text{PbI}_{3-x}\text{Cl}_x$ nanosheet arrays. In the end, the $\text{CH}_3\text{NH}_3\text{PbI}_{3-x}\text{Cl}_x$ nanosheet arrays were gently washed in isopropanol and dried under a stream of nitrogen flow.

Structural characterization. The PXRD data of the nanosheet arrays were acquired on a Rigaku SmartLab diffractometer in the 2-theta range of 10°-60° with an interval of 0.02°. The scanning electron microscope (SEM) images were collected on Nova NanoSEM 650. The Energy-dispersive X-ray microanalysis (EDX) equipped in the SEM system was used to characterize the component information of the material. The nanosheet sample for transmission electron microscope (TEM) was dry-transferred and dispersed onto a copper grid. The TEM images were acquired on a JEM-2010 (Japanese electronic optical co, LTD) TEM at an operating voltage of 120 kV. Energy-dispersive X-ray spectroscopy (EDX) measurement was also performed from this integrated TEM equipped with an Oxford Inca EDX with a (I+Cl)/Pb ratio of 3.01, which is better consistent with the $\text{CH}_3\text{NH}_3\text{PbI}_x\text{Cl}_{3-x}$ stoichiometry. X-ray photoelectron spectroscopy (XPS) measurement was carried out using an ESCALAB 250Xi (Thermo Fisher) to give out peaks position as the humidity variation. The absorption spectra of as-grown perovskite samples were measured at room temperature on a double beam ultra violet (UV) spectrophotometer of TU1950. The position of energy levels in perovskite

nanosheet were achieved by ultraviolet photoemission spectroscopy (UPS, Kratos AXIS UL TRA DLD).

Device fabrication. The as-prepared perovskite nanosheet arrays were transferred to the glove box, annealed at 70 °C for 20 min and followed by thermal evaporation of 200 nm silver as the terminal electrode. The center area between the two terminal electrodes was defined as the active area for water sensing. The thin film was fabricated by spin coating the perovskite precursor ($\text{CH}_3\text{NH}_3\text{PbI}_{0.2}\text{Cl}_{2.8}$ 10wt% in DMSO) on PEDOT:PSS/Glass substrate at 2000 rpm, and then annealed at 100 °C for 20 min and followed by thermal evaporation of 200 nm silver as the terminal electrode.

Perovskite nanosheet arrays humidity sensor (PNSAHS) characterization. The current-voltage curves were measured using a Model 2450 SourceMeter of Keithley Instruments. The resistance was calculated by the slope which was obtained from the linear fit of current-voltage curves. The humidity environment was controlled by a HSB-50 L temperature and humidity test chamber (Hefei bianco environmental testing equipment co., LTD). The real-time current response to the humidity was tested by a CHI660E electrochemical workstation. The Mott-Schottky plots were also obtained from CH660E. AC oscillating amplitude was controlled as low as 5 mV to maintain the linearity of the response and the measuring frequency was set as 1000 Hz. The doping level N can be extracted from the equation¹:

$$N \text{ (doping density)} = \frac{2}{\text{slope}(a) \cdot e \cdot \varepsilon \cdot \varepsilon_0} \text{ (cm}^{-3}\text{)}.$$

In the equation, the slope (a) can be obtained from the Mott-Schottky plots. In addition, e and ε_0 are the elementary charge and permittivity in free space, respectively. The dielectric constant, ε , was set as 23.9² due to the fact that the material is mainly $\text{CH}_3\text{NH}_3\text{PbCl}_3$. The responses of PNSAHS to the various surrounding atmospheres were characterized by a Model 2450 SourceMeter of Keithley Instruments and a test tube. The different atmospheres were controlled by adding 5 mL organic chemical solvents (methanol, acetone, toluene, chlorobenzene, trichloromethane, ammonium hydroxide) in test tube. The PNSAHS was placed in the test tube by using the parafilm to seal it. When the volatile velocity was steady, the current-voltage test was performed. In addition, we also put the sensor in a sealed chamber (300 mL), and then injected different volumes of gases like CO , O_2 and H_2 to measure the responses of the sensor in different volume ratios ($V_{\text{gas}}/V_{\text{air}}$).

Computational details: The calculations were performed by using the project augmented plane-wave (PAW) method within the framework of DFT in the Vienna ab initio Simulation Package (VASP). The electron exchange and correlation were described by the generalized gradient approximation (GGA) of Perdew, Burke, and Ernzerhof (PBE) functional. The cutoff energy for the plane-wave basis set was set to

450 eV. A supercell composed of $(1 \times 2 \times 2)$ unit cells was constructed in this work to adjust the concentration of adsorbed H_2O molecules. The first Brillouin zone was sampled with a $(9 \times 9 \times 9)$ Monkhorst–Pack grid for relaxation of $\text{CH}_3\text{NH}_3\text{PbCl}_3$ unit cell. A $(5 \times 5 \times 9)$ Monkhorst–Pack grid was used for relaxation of the supercells employed in this work. All of the structures are fully relaxed with a force tolerance of 0.01 eV/\AA .

Section 2. Additional Figures and Discussions

To better understand the growth process and mechanism of the perovskite nanosheets, we have monitored the appearance evolution of as-grown perovskite samples (Fig. S1), surface morphology (Fig. S2A-I), the normalized atom variation ratios (Fig. S3) and PXRD patterns (Fig. S4) as the reaction time increases. We have also measured the SEM images of the as-grown $\text{CH}_3\text{NH}_3\text{PbI}_{3-x}\text{Cl}_x$ morphology (Fig. S5) evolution with different reaction concentration ratios of $\text{CH}_3\text{NH}_3\text{Cl}:\text{CH}_3\text{NH}_3\text{I}$ /isopropanol.

As displayed in the series of photographs taken on the as-grown perovskite samples at different reaction time (Fig. S1), the color first looks transparent like the as-deposited PbAc_2 thin film, several minutes later it turns to white very quickly, due to the consumption of PbAc_2 to form dispersed perovskite nanocrystals on the surface (Fig. S2A-C). These dispersed nanocrystals could not only serve as the nucleation center, but also allow the complete conversion of PbAc_2 to perovskite nanostructures.

In the initial growing step of nanostructures like nanowires and nanosheets, the crystal formation could be controlled by dislocation-driven growth mechanism, where screw dislocation defects provide self-perpetuating growth steps to enable the anisotropic growth of various nanomaterials at low supersaturation as reported by the references.^{3,4} As the growing time increases, however, the nanostructures with a high aspect ratio like nanowires and nanodots disappear and the nanosheets grow larger and thicker (Fig. S2D-I). Obviously, this is governed by the Ostwald ripening process, where the unstable smaller clusters dissolve and contribute their monomers to the growth of larger clusters by means of the molecular diffusion.⁵ Fig. S3 shows the corresponding normalized atom% variation ratios of nanostructure with the reaction time. In the first two hours, the contents of C, O and Pb decrease while those of Cl, I and N increase, indicative of the consumption of PbAc_2 and the formation of $\text{CH}_3\text{NH}_3\text{PbI}_{3-x}\text{Cl}_x$. As the time being prolonged, the contents of these elements become stable but the morphologies of the nanostructures shown in the SEM images still change. This supports the Ostwald ripening process in the second step of crystal growth. In addition, the formation of perovskite materials at the cost of the PbAc_2 could also be observed in the PXRD patterns as shown in Fig. S4.

Interestingly, we observe that the mixed halide concentration ratio of $\text{CH}_3\text{NH}_3\text{Cl}$ and $\text{CH}_3\text{NH}_3\text{I}$ plays an important role in the formation of some specially shaped nanomaterials and only the near 1:1 halide ratio and the special concentration could grow the nanosheet arrays with the uniform morphology, as indicated in Fig. S5. The EDX spectrum of a single nanosheet is shown in Fig. S6 and the composition of the elements could be estimated as $\text{CH}_3\text{NH}_3\text{PbI}_{0.2}\text{Cl}_{2.8}$, indicating that the perovskite is

chlorine based. Fig. S7 shows the absorption spectrum of the as-grown nanostructures and the band gap of 2.97 eV could be concluded.

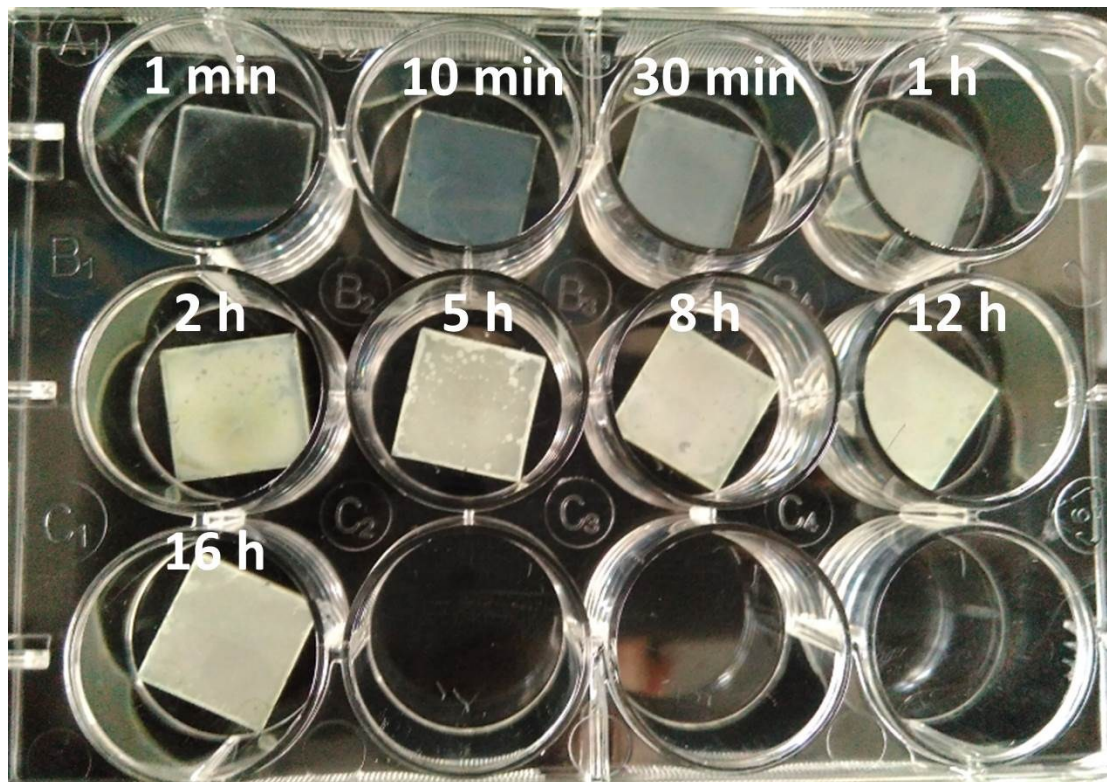


Fig. S1. Photograph of as-grown $\text{CH}_3\text{NH}_3\text{PbI}_{3-x}\text{Cl}_x$ samples on glass substrates after reaction at different time.

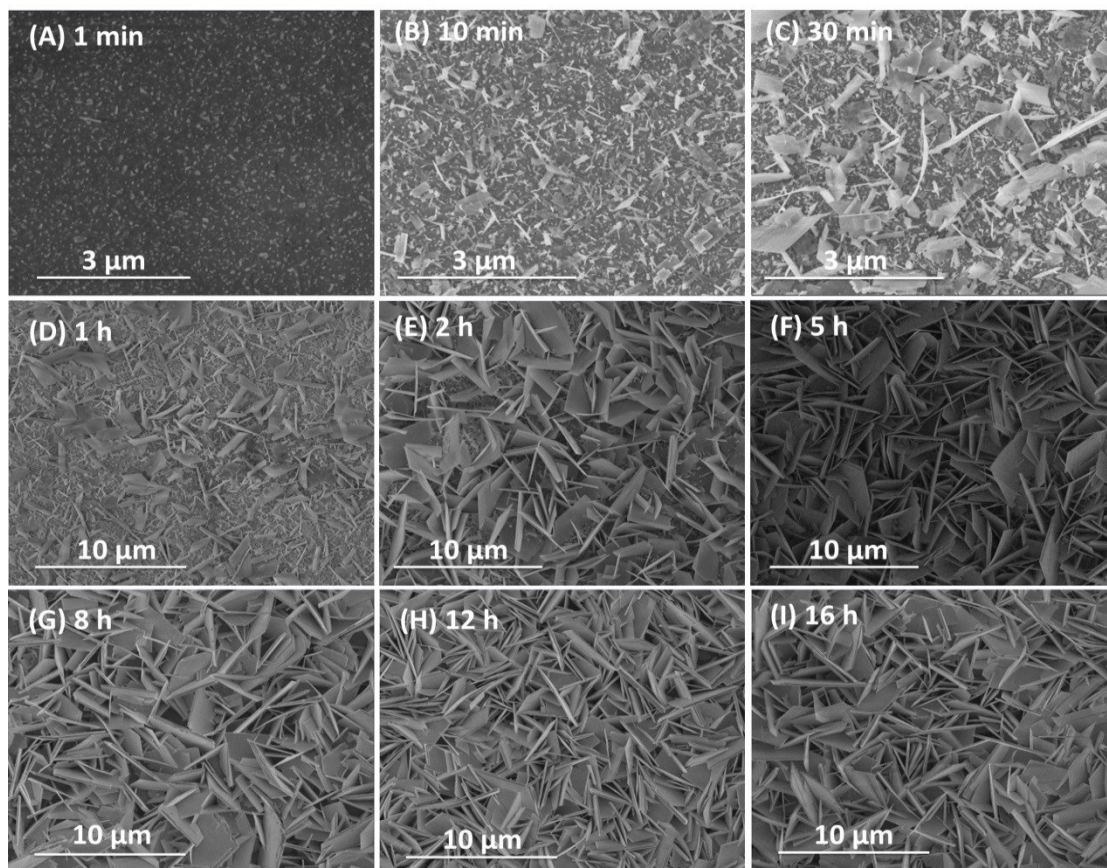


Fig. S2. SEM images of the as-grown $\text{CH}_3\text{NH}_3\text{PbI}_{3-x}\text{Cl}_x$ morphology evolution with a reaction time at 1 min, 10 min, 30 min, 1 h, 2 h, 5 h, 8 h, 12 h, 16 h, respectively.

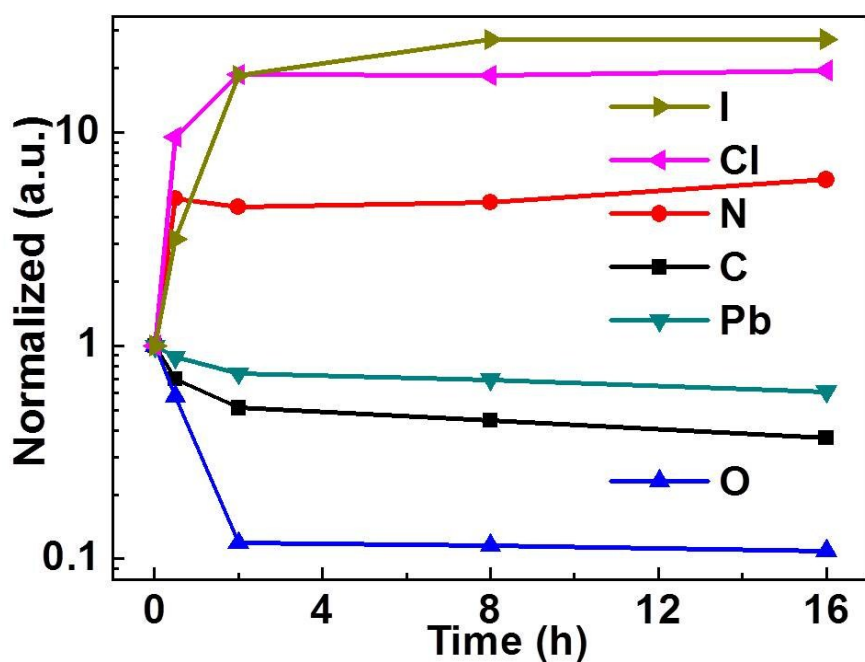


Fig. S3. The normalized atom variation ratios of $\text{CH}_3\text{NH}_3\text{PbI}_{3-x}\text{Cl}_x$ samples with the changing reaction time.

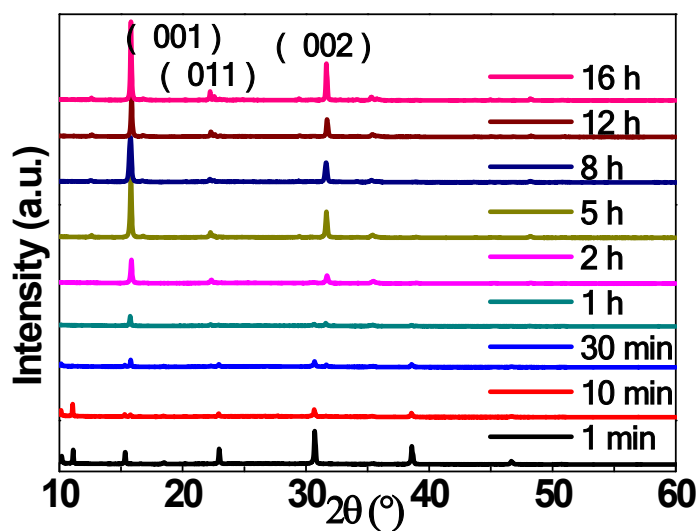


Fig. S4. PXRD patterns of the as-grown $\text{CH}_3\text{NH}_3\text{PbI}_{3-x}\text{Cl}_x$ nanosheet arrays at different reaction time.

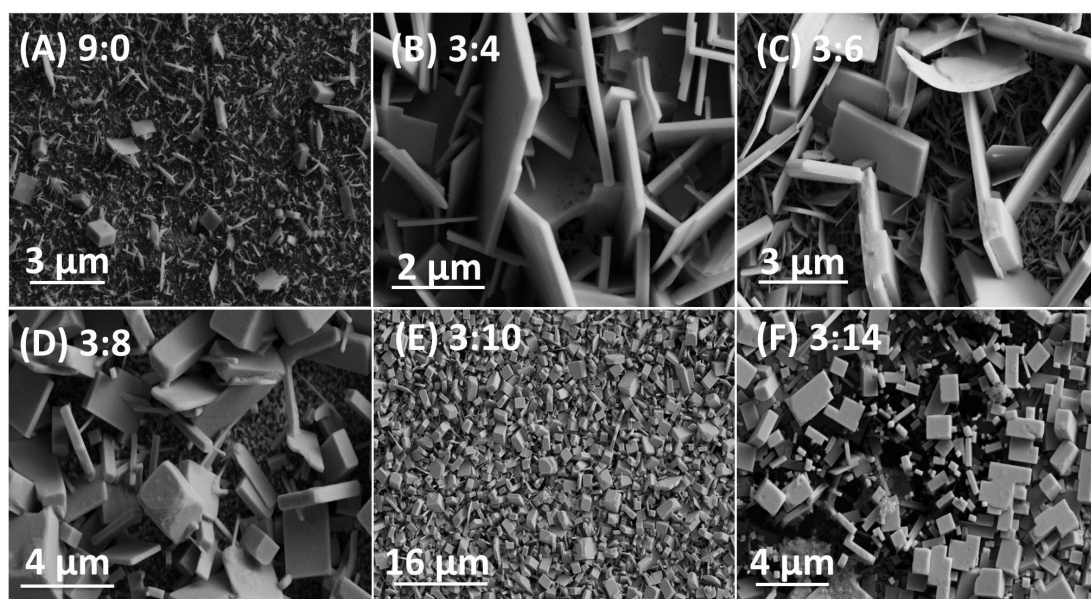


Fig. S5. SEM images of the as-grown $\text{CH}_3\text{NH}_3\text{PbI}_{3-x}\text{Cl}_x$ morphology evolution with different concentration ratios of $\text{CH}_3\text{NH}_3\text{Cl}:\text{CH}_3\text{NH}_3\text{I}$ /isopropanol solution.

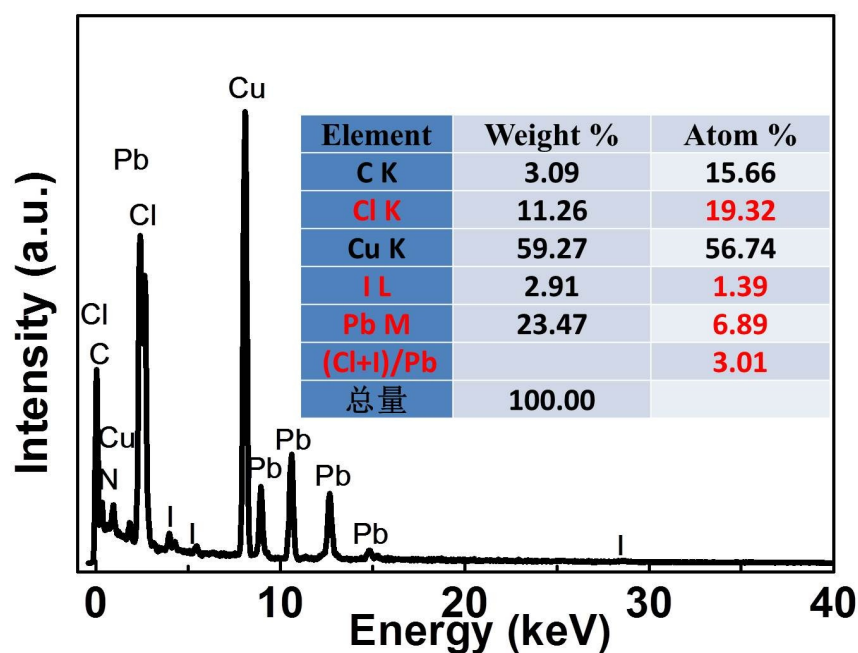


Fig. S6. A representative EDX spectrum of a single nanosheet onto a copper grid. The insert table is the corresponding quantitative elemental analysis of a single nanosheet which gives a (I+Cl)/Pb ratio of 3.01, in good agreement with a $\text{CH}_3\text{NH}_3\text{PbI}_{3-x}\text{Cl}_x$ stoichiometry.

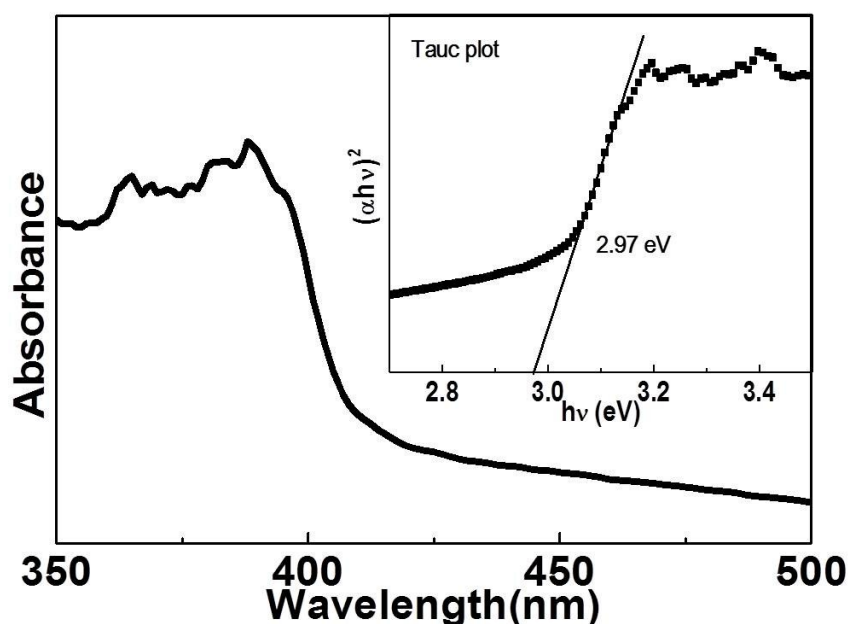


Fig. S7. The absorption spectra of as-grown $\text{CH}_3\text{NH}_3\text{PbI}_{3-x}\text{Cl}_x$ nanosheet. From the converted Tauc plot (inset) we got the optical band gap to be 2.97 eV. This bandgap is narrower than previous report,⁶ possibly due to the iodine doping.

Section 3. Discussion on the influence of humidity on the sensing performance

DFT calculated band structures of the perovskite nanosheets are shown in Fig. S8. With more water molecules in the structure, the band gap value does not show obvious change, though the density of states in the valence and conduction band changes prominently.

The responses of the devices in lower humidity conditions are given in Fig. S9. The resistance still presents an obvious change from $1.40\text{E}9 \ \Omega$ to $3.22\text{E}8 \ \Omega$, when the humidity is tuned from around 0 (in glove box, water content $<1 \text{ ppm}$) to 27% RH. This indicates that the device can also work in the condition with lower humidity values. When exposed in the condition with humidity higher than 90% RH, the nanostructure arrays begin to decompose as shown in Fig. S10.

To check the reversibility of the devices, the structure was first exposed to the conditions with different humidity and then experienced XRD measurement in ambient with humidity of 30% RH. As shown in Fig. S11a, all the spectra show the same set of diffraction peaks. These peaks could be indexed to the lattice planes of cubic $\text{CH}_3\text{NH}_3\text{PbCl}_3$ crystal structures without any doping impurity phases (ex. PbCl_2 , PbI_2 or PbAc_2), demonstrating that the perovskite structure is reversible after the RH processing. The characteristic diffraction peaks (001) and (002) also get enhanced in the intensity as the RH increases (similar to the annealing procedure), thus implying that a suitable RH is responsible to the good crystallinity of the perovskite nanosheets. This is in good agreement with the previous report.⁷ Fig. S11b gives the XPS full scan of the set of samples and the main peaks of the perovskite material are nearly invariant

in processing at different RH atmospheres. The tiny O 1s peak is of high possibility to be from the absorbed oxygen or other oxygen involved contaminations.⁸⁻¹⁰

Fig. S12a shows the resolved Pb 4f peaks of these samples. In comparison with the sample in the ambient atmosphere, though the peaks of the Pb 4f shift slightly for the samples that exposed to the humidity atmospheres with 60% RH and 90% RH, respectively, we could not observe the Pb 4f peaks that belong to PbCl₂ or PbI₂,¹¹ even for the samples that exposed to the 90% RH atmosphere for 2 h. This could also be supported by the resolved Cl 2p (Fig. S12b) and I 3d (Fig. S12c) peaks.

To check the stability of the nanostructure array, we measured the samples after continuous XPS measurements. As shown in Fig. S13, both elemental ratio and XRD pattern of the nanostructure do not show any obvious change, thus indicating the good stability towards XPS measurement.

To investigate more on the influence of humidity on the conductivity of the sensing device, Mott-Schottky plots were measured and shown in Fig. S14. With the increase of humidity in the exposed ambient, the slopes of plots show a decreasing feature and this indicates that the doping density of the perovskite nanostructure increases accordingly. The calculated doping density is shown in Table S1 and the increasing doping density is responsible for the increased conductivity and the decreased resistance.

To show the advantage of our devices based on nanostructure arrays, we also fabricated sensor device based on flat perovskite structure. As demonstrated in Fig. S15, as we tune the humidity from 30% to 90% RH, the resistance only shows a change of around 2 folds. This value is several orders of magnitudes lower than that from the devices based on nanostructure arrays.

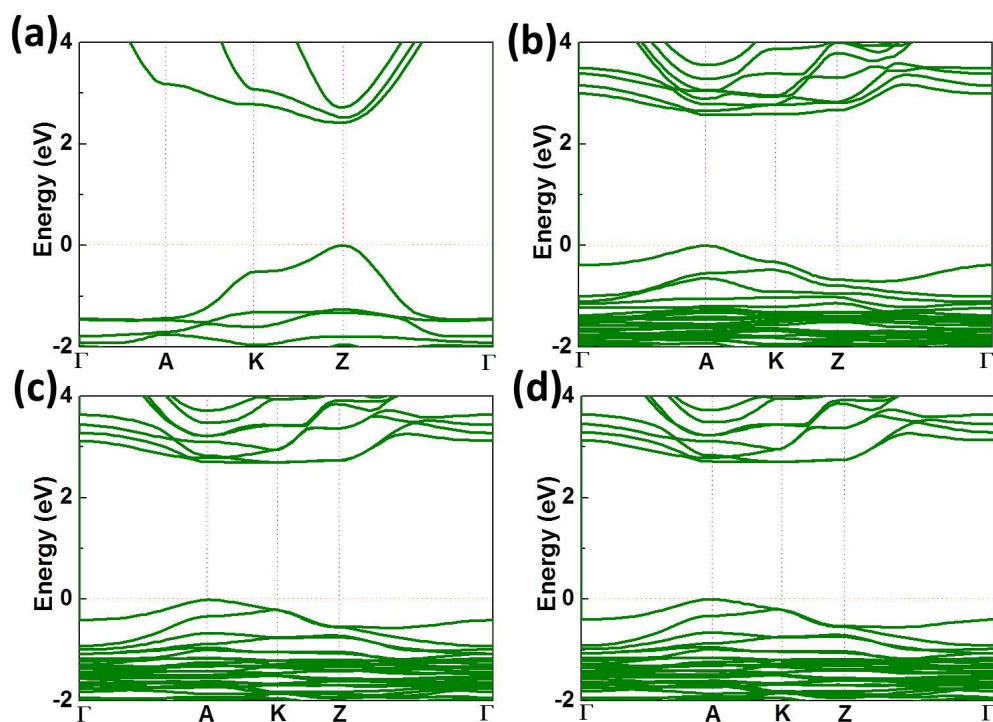


Fig. S8. (a) Calculated band structure of perovskite $\text{CH}_3\text{NH}_3\text{PbCl}_3$ without absorbing water molecule. (b-d) Calculated band structure of perovskite $\text{CH}_3\text{NH}_3\text{PbCl}_3$ supercell with absorbing 1, 2 and 4 water molecules.

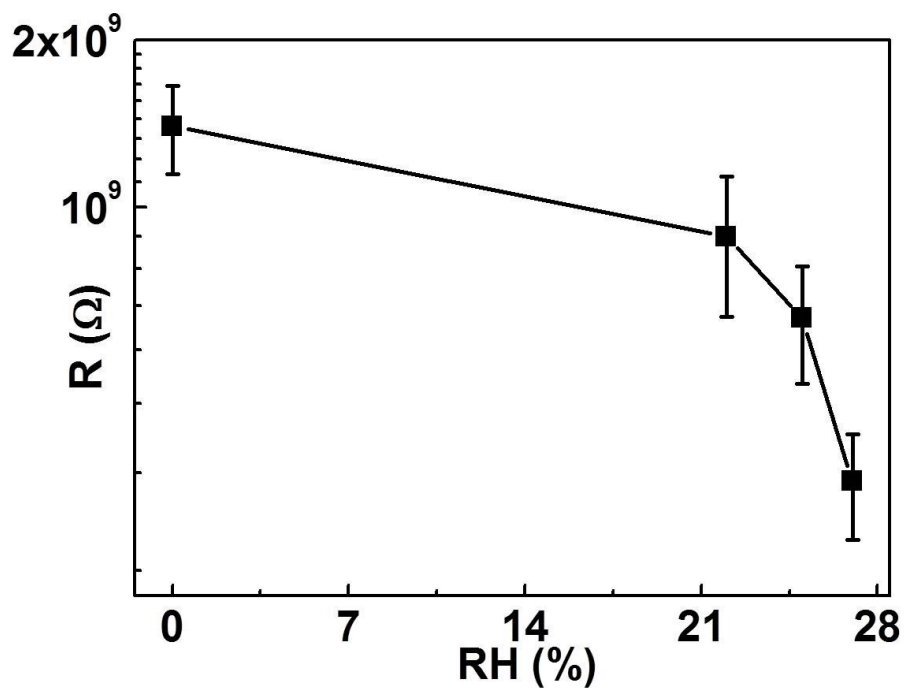


Fig. S9. The resistance changing of PNSAHS in the low RH environment.

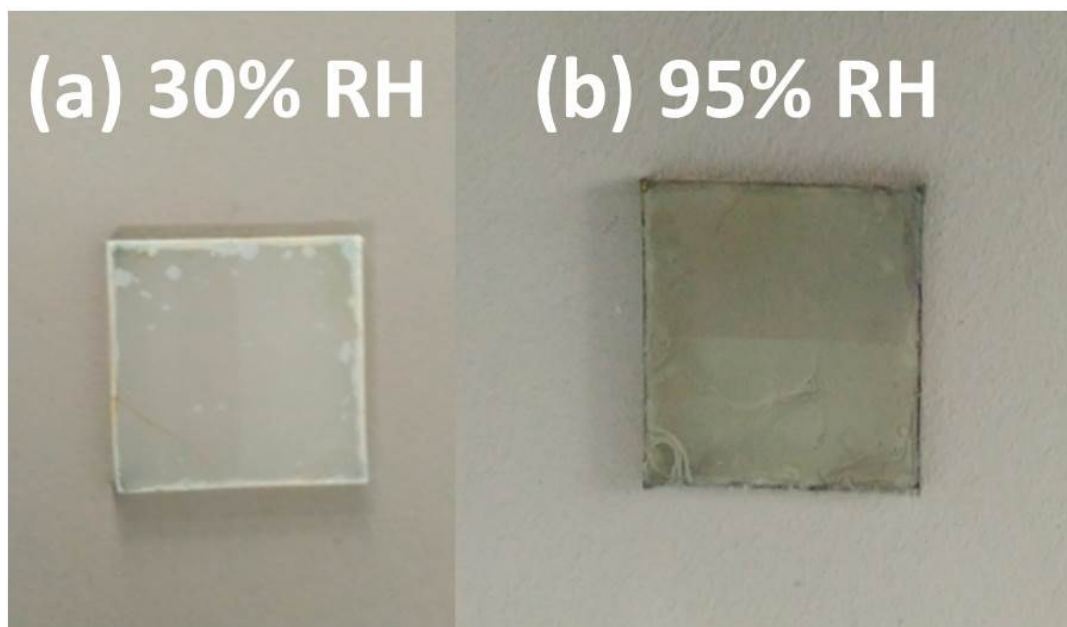


Fig. S10. Photographs of as-grown $\text{CH}_3\text{NH}_3\text{PbI}_{3-x}\text{Cl}_x$ samples at ambient environment (a) and 95% RH environment (b).

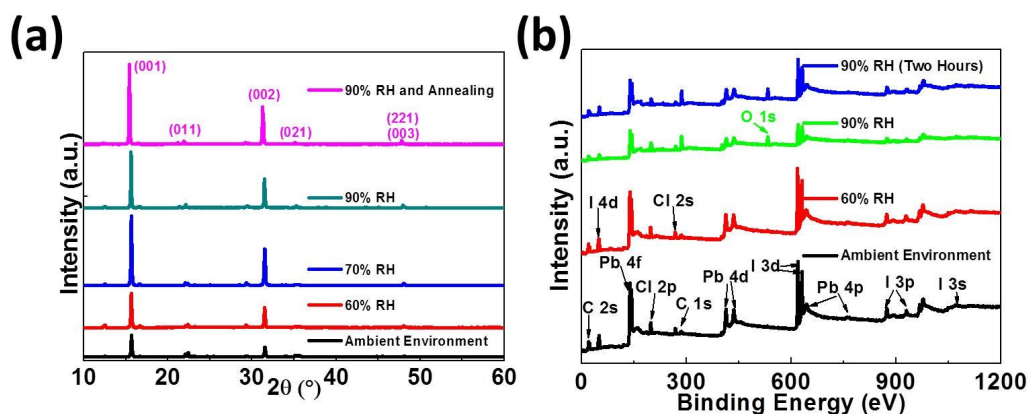


Fig. S11. PXRD spectra (a) and XPS survey spectra (b) of as-grown perovskite nanosheet in processing at different RH atmospheres. The RH processing time is half an hour for the unlabeled lines. The tinny O 1s peak is of high possibility to be from the absorbed oxygen or other oxygen involved contaminations⁸⁻¹⁰.

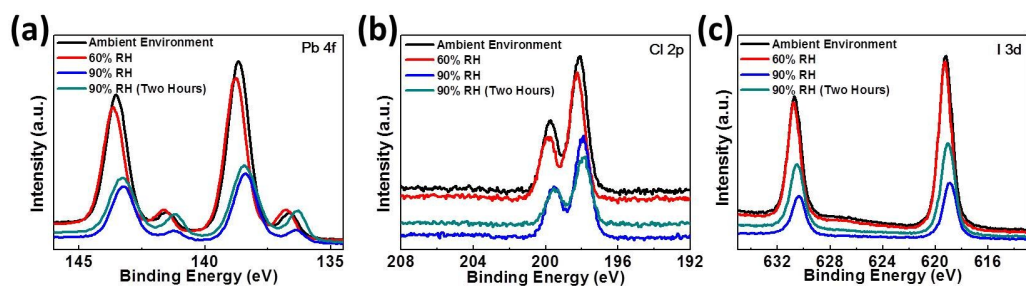


Fig. S12. High resolution XPS spectra of different elemental core level. (a) Pb 4f, (b) Cl 2p and (c) I 3d core level spectra.

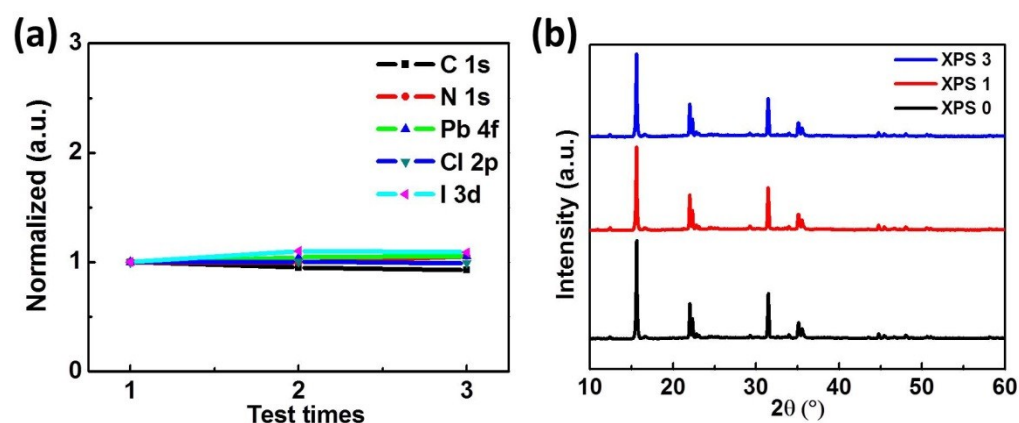


Fig. S13. (a) The normalized element changing of $\text{CH}_3\text{NH}_3\text{PbI}_{3-x}\text{Cl}_x$ at different XPS test times. (b) The PXRD patterns of $\text{CH}_3\text{NH}_3\text{PbI}_{3-x}\text{Cl}_x$ after different XPS test times.

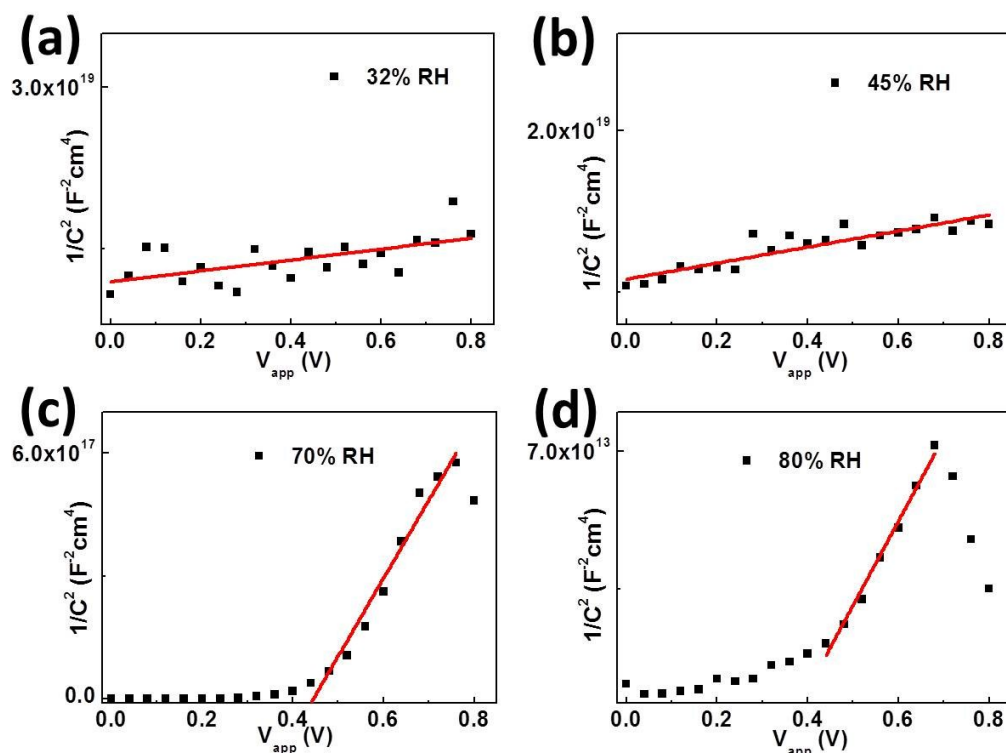


Fig. S14. Mott-Schottky plots of PNSAHS in different RH atmospheres. The linear fit is shown as the red line from which we get the slope and extract the doping level N (Table 1).

RH (%)	32	45	70	80
N (cm^{-3})	1.17E12	1.19E12	3.10E12	2.76E16

Table S1. The doping level N is extracted from the Mott-Schottky analysis of PNSAHS in different RH atmosphere.

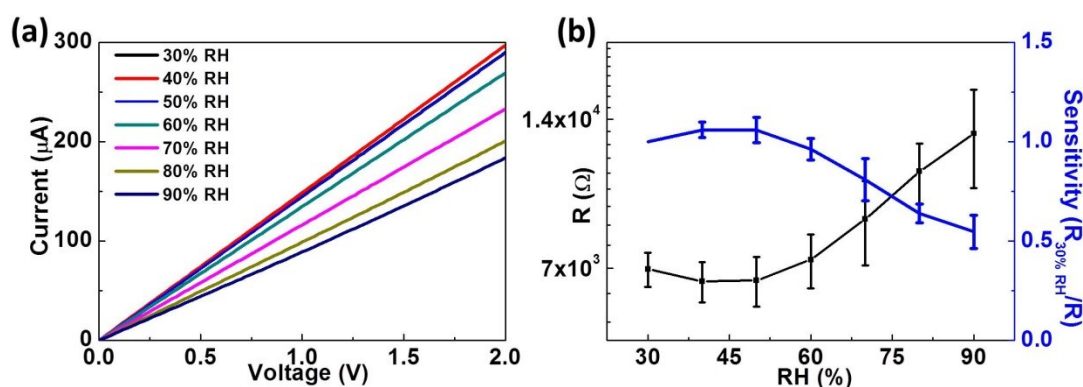


Fig. S15. (a) I-V curves of perovskite $\text{CH}_3\text{NH}_3\text{PbI}_{0.2}\text{Cl}_{2.8}$ thin film in different RH atmospheres from low humidity (30% RH) to 90% RH at 27 °C. (b) The average resistance of perovskite $\text{CH}_3\text{NH}_3\text{PbI}_{0.2}\text{Cl}_{2.8}$ thin film in different RH gases (black line) and the resistance response sensitivity which is defined by $R_{30\% \text{ RH}}/R$ (blue line).

Section 4. Discussion on the specificity of the devices

As shown in Fig. S16, the resistance ratio of R/R_0 shows different responses towards the atmospheres with different molecules. The ratio presents a declined feature when the samples are exposed to methanol (Me), chlorobenzene (Chl) and ammonium hydroxide (AmHy). This is similar to the phenomena in water exposure, but the declining extent is highly dependent on the nature of the molecules, like the electron injection capability to the perovskite and the diffusion efficiency of the molecule in the perovskite. However, when exposed to the acetone (Ace), toluene (Tol) and trichloromethane (Tri) atmospheres, the ratio increases. This could be possibly from the different charge transfers between the molecules and the perovskite. All these results indicate a good sensing property of the prepared perovskite nanosheet arrays, not only for humidity sensing but also for organic molecule sensing.

In addition, we also measured the responses of our device towards CO , O_2 and H_2 . As shown in Fig. S17, these responses are not as large as those measured in methanol or other mentioned vapors, but still present a relative selectivity.

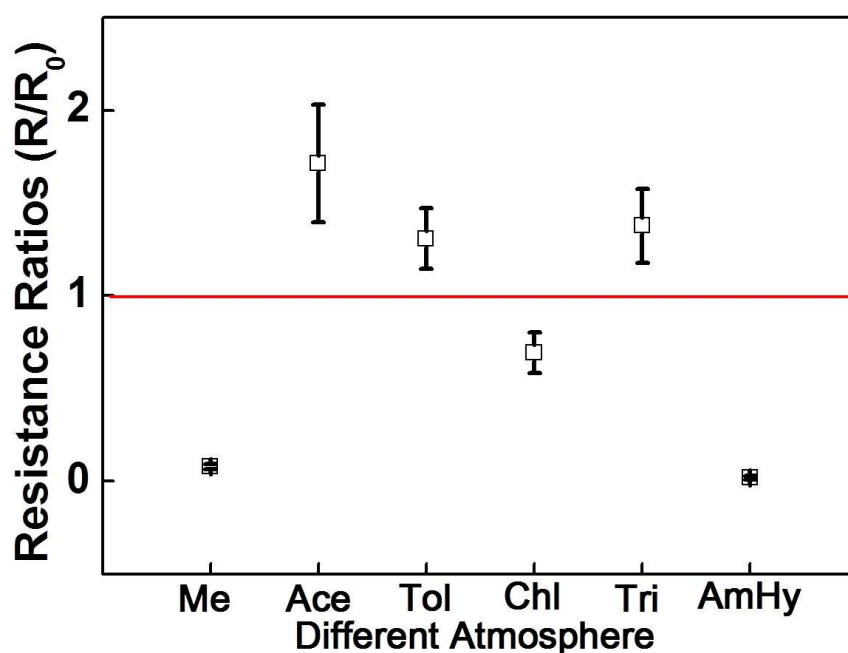


Fig. S16. The resistance changing ratio of PNSAHS upon exposure toward different ambient atmospheres. The ambient environment was around 44% RH at 26 °C.

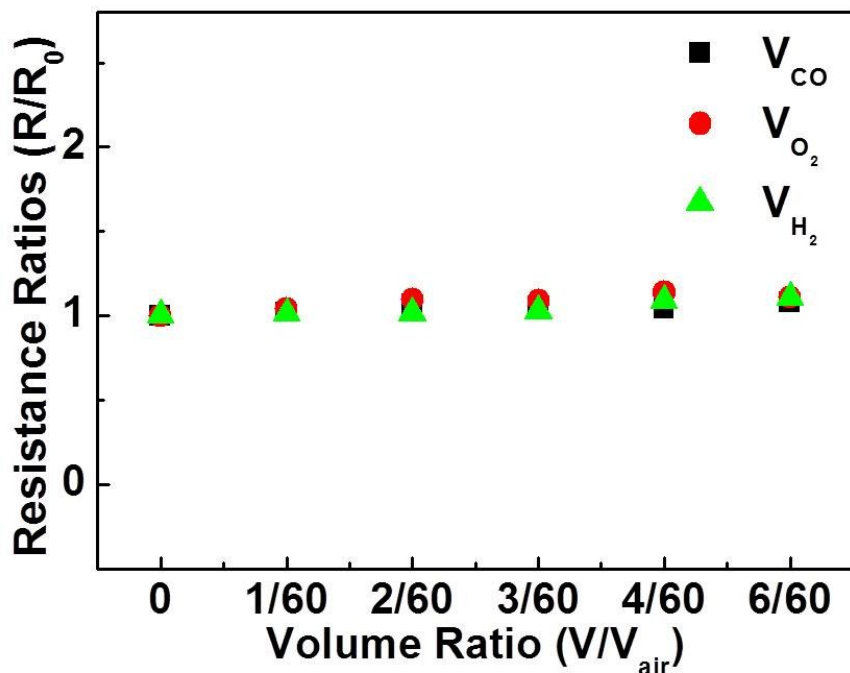


Fig. S17. The resistance changing ratio of PNSAHS upon exposure toward different gases.

References

1. A. Guerrero, L. F. Marchesi, P. P. Boix, S. Ruiz-Raga, T. Ripolles-Sanchis, G. Garcia-Belmonte and J. Bisquert, *ACS Nano*, 2012, **6**, 3453-3460.
2. G. Maculan, A. D. Sheikh, A. L. Abdelhady, M. I. Saidaminov, M. A. Haque, B. Murali, E. Alarousu, O. F. Mohammed, T. Wu and O. M. Bakr, *J. Phys. Chem. Lett.*, 2015, **6**, 3781-3786.
3. H. Zhu, Y. Fu, F. Meng, X. Wu, Z. Gong, Q. Ding, M. V. Gustafsson, M. T. Trinh, S. Jin and X. Y. Zhu, *Nat Mater*, 2015, **14**, 636-642.
4. F. Meng, S. A. Morin, A. Forticaux and S. Jin, *Acc Chem Res*, 2013, **46**, 1616-1626.
5. B. J. M. Giridhar Madras, *J. Chem. Phys.*, 2002, **117**, 8042-8049.
6. A. Sadhanala, S. Ahmad, B. Zhao, N. Giesbrecht, P. M. Pearce, F. Deschler, R. L. Hoyer, K. C. Godel, T. Bein, P. Docampo, S. E. Dutton, M. F. De Volder and R. H. Friend, *Nano Lett.*, 2015, **15**, 6095-6101.
7. M. K. Gangishetty, R. W. Scott and T. L. Kelly, *Nanoscale*, 2016, **8**, 6300-6307.
8. H. Yu, F. Wang, F. Xie, W. Li, J. Chen and N. Zhao, *Adv. Funct. Mater.*, 2014, **24**, 7102-7108.
9. L. Hu, G. Shao, T. Jiang, D. Li, X. Lv, H. Wang, X. Liu, H. Song, J. Tang and H. Liu, *ACS Appl Mater Inter.*, 2015, **7**, 25113-25120.
10. H. Kim, H. Cho, J. H. Heo, T. S. Kim, N. Myoung, C. L. Lee, S. H. Im and T. W. Lee, *Adv Mater*, 2015, **27**, 1248-1254.
11. B. Philippe, B.-W. Park, R. Lindblad, J. Oscarsson, S. Ahmadi, E. M. J. Johansson and H. Rensmo, *Chem. Mater*, 2015, **27**, 1720-1731.